



Investigating the effects of Fourier-based particle shape on the shear behaviors of rockfill material via DEM

Zhihong Nie¹ · Yangui Zhu¹ · Xiang Wang¹ · Jian Gong¹

Received: 21 June 2018 / Published online: 4 March 2019
© Springer-Verlag GmbH Germany, part of Springer Nature 2019

Abstract

This report investigates the effects of Fourier-based particle shape on the macroscopic and microscopic shear responses of rockfill material via a series of numerical biaxial compression tests. The multi-disk method is employed to model two-dimensional irregular rockfill particles. The macroscopic characteristics, including the shear strength and the dilatancy response, and the microscopic characteristics, including the contact force, the coordination number and the sliding contact, are examined. Then, detailed analyses of the fabric anisotropy of the entire contact network empower us to understand the microscopic mechanisms that lead to the dependency of the shear strength on particle shape. Subsequently, analyses concerning the fabric anisotropy of the strong and weak contact networks are carried out. It is found that the macroscopic stress ratio exhibits a linear pattern with the anisotropic coefficient of contacts in the strong contact network, and that the slope depends on particle shape.

Keywords Fourier-based · Particle shape · Biaxial compression test · Micro-mechanics · Fabric anisotropy

1 Introduction

Rockfill material, which is derived from a mechanical process, e.g., the blast and breakage of a rock mass, consists of angular- or sub-angular-shaped particles. In general, the particle size of rockfill material is quite large, and the maximum size may exceed 1 m in some situations. Rockfill material is widely used in geotechnical engineering structures such as highway and railway subgrades, earth and rockfill dams. The shear strength and deformation mechanism of rockfill material are of interest to many researchers because of their significance in engineering. The particle shape of rockfill material has been viewed as a crucial factor that influences its macroscopic mechanical and physical properties [1–3]. Therefore, several attempts have been conducted to investigate the shape effects on the complicated mechanical behaviors of rockfill material through laboratory experiments and field tests [4–6]. However, while these experimental tests have provided insight into the effects of particle shape by means of ample macroscale data, microscale data

are insufficient. Moreover, it is very difficult to precisely control the shapes of particles in test groups during common experimental tests. Accordingly, to understand the mechanism from a microscale particle level and accurately control particle shapes, many investigators have been inclined to perform numerical simulations.

The discrete element method [7] (DEM) has enabled researchers to study the mechanical behaviors of granular material from a particle level [8–16]. In this method, particles are often idealized as circles or spheres due to the requirement of computational efficiency. Nevertheless, particles modeled as circles or spheres are far from an adequate description of realistic particles in shape. To date, other non-circular and non-spherical geometries, such as polygons [17], polyhedrons [18], ellipses [19], ellipsoids [20], and superballs [21], have also been utilized, but none of them provide a precise description of the intricate particle shape. At present, the geometrical descriptors of shape quantification, including sphericity [22, 23], aspect ratio [24, 25], elongation [20, 26], roundness [27–29], angularity [30, 31], roughness [32, 33] and so forth, have been used to describe particle shape, but these descriptors have not been adequately systematic and precise.

Some investigators have attempted to offer a general framework that could describe and generate realistic particle shapes.

✉ Jian Gong
gj_csu@hotmail.com

¹ School of Civil Engineering, Central South University, Changsha 410075, China

The Fourier-based method was used to describe the shapes of particles in [34–36], and was suggested in [37–39] for generating realistic sand particles. Differentiating from those traditional shape descriptors, the utilization of the Fourier-based method makes it possible to both quantitatively describe and randomly generate particle shapes precisely on the basis of a statistical and uniform approach. Liu and Zhao [40] studied the influence of particle shape on the mechanical properties of sand particles based on this method. Note that these sand particles might have obviously different elongations and the shear state might not reach the critical state.

The primary purpose of this work is to offer comprehensive analyses of the effects of Fourier-based particle shape on the macro- and micro-mechanical behaviors of rockfill material at different states using DEM. Particularly, all particles are ensured to have nearly equal elongations. This work is organized as follows. First, brief introductions of methodologies about the Fourier-based random generation of particle shape and DEM modeling are given. Then, the macroscopic responses, including the shear strength and dilatancy, are presented. Afterwards, microscopic responses such as the contact force, the coordination number and the sliding contact are investigated. In addition, the fabric anisotropy of the entire contact network and the fabric anisotropy of the strong and weak contact networks are analyzed. Finally, the main conclusions of the work are provided.

2 Methodology

2.1 Fourier-based random generation of particle shape

The Fourier-based method was originally proposed by Ehrlich and Weinberg [34] to characterize particle shape through a Fourier series. On the basis of this method, the Fourier descriptor D_n was presented by Mollon and Zhao [37] to describe the particle shape of sand. For a given 2D particle contour, D_n can be defined as follows [37]:

$$D_n = \frac{\sqrt{A_n^2 + B_n^2}}{r_0} \quad (1)$$

where A_n and B_n represent the Fourier spectrum of the particle contour which is discretized into a number of points in polar coordinates, and r_0 is the average length of the line segments connecting the coordinate origin and the discrete points. The shape of the particle contour can be described by Fourier descriptors D_0 to D_{64} [31]. $D_0=1$ and $D_1=0$ are fixed. D_2 characterizes the elongation of the particle shape. D_3 to D_7 describe the irregularity of the particle shape. D_8 to D_{64} represent the small-scale variation in the particle shape,

i.e., roughness. Following Mollon and Zhao [37], D_3 to D_7 and D_8 to D_{64} have empirical expressions as follows:

$$D_n = 2^{-2\log_2(n/3)+\log_2(D_3)} \quad \text{for } 3 \leq n < 8 \quad (2)$$

$$D_n = 2^{-2\log_2(n/8)+\log_2(D_8)} \quad \text{for } 8 \leq n \leq 64 \quad (3)$$

Therefore, D_0 to D_{64} are determinate when D_2 , D_3 and D_8 are given. Namely, the particle shape is controlled by D_2 , D_3 and D_8 .

When D_0 to D_{64} are determinate, the contour of a required particle can be generated by the following equations [31]:

$$A_n = r_0 \cdot D_n \cdot \sin \delta_n \quad (4)$$

$$B_n = r_0 \cdot D_n \cdot \cos \delta_n \quad (5)$$

$$r(\theta) = r_0 + \sum_{n=1}^{64} [A_n \cos(n\theta) + B_n \sin(n\theta)] \quad (6)$$

where δ_n is the phase angle; $r(\theta)$ is the length of the line segment connecting the coordinate origin and the discrete contour point; θ is the angle of the discrete contour point in polar coordinates, and it is in the range of $[0, 2\pi]$. To generate a number of particles that have diverse shapes but share the identical D_n , δ_n is chosen randomly in $[-\pi, \pi]$.

The particle shape of granular material can be quantified using certain descriptors, such as roundness (RO), circularity (CI), and regularity (RE), which can be defined as follows [37]:

$$RO = \sum R_c / (n_c \times R_{ins}) \quad (7)$$

$$CI = \sqrt{R_{ins}/R_{cir}} \quad (8)$$

$$RE = \log(P/(P - P_{con})) \quad (9)$$

where R_c is the radius of the circle approximating the particle contour, and n_c is the number of all these circles; R_{ins} and R_{cir} denote the radii of the maximum inscribed circle and the circumscribed circle of the particle contour, respectively; P and P_{con} represent the perimeter and the convex perimeter of the particle contour, respectively. The schematic diagram for the calculation of RO , CI and RE of a particle is illustrated in Fig. 1. Previous studies [25, 41–43] have focused on the effects of elongation (reflected by D_2) and roughness (reflected by D_8) on the shear behaviors of granular material. However, the effects of RO , CI and RE (reflected by D_3) on the macroscopic and microscopic characteristics of rockfill material are still unclear. This is the motivation of this work, wherein we conducted grain-scale modeling using the DEM, aiming at exploring the effects of D_3 on the shear behaviors of rockfill material. In this study, $D_2=D_8=0$, and D_3 values are 0.00, 0.015, 0.03, 0.06, 0.09, 0.12, 0.15 and 0.18. According to Mollon and Zhao [37], Fig. 2 illustrates the

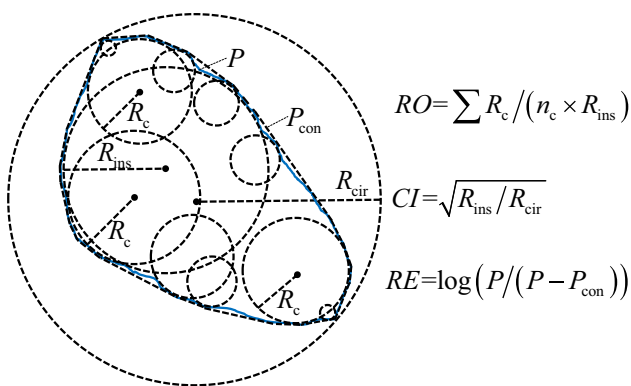


Fig. 1 A schematic diagram for the calculation of the particle shape descriptors: RO , CI and RE

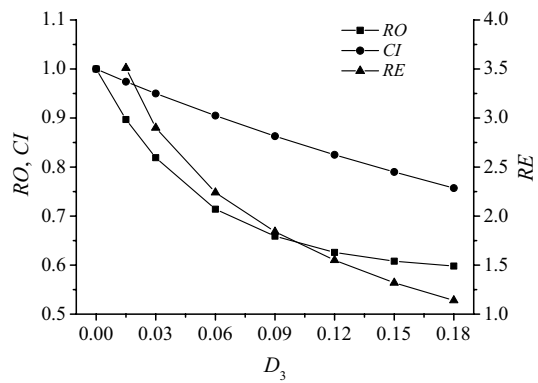


Fig. 2 Relationships between the mean value of the shape descriptor (RO , CI and RE) and D_3 when $D_2=D_8=0$

relationships between RO , CI , RE and D_3 when $D_2=D_8=0$. Clearly, as D_3 increases from 0.00 to 0.18, RO gradually decreases from 1 to 0.598; CI gradually decreases from 1

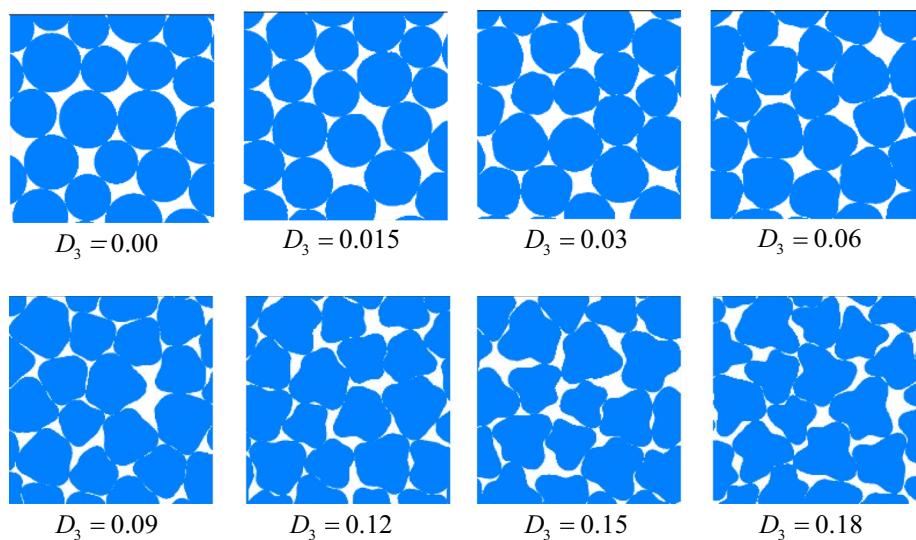
to 0.757; RE gradually decreases from positive infinity to 1.14. Note that when $D_2=D_8=0$, and D_3 equals 0.00, 0.015, 0.03, 0.06, 0.09, 0.12, 0.15 and 0.18, the elongations of the Fourier-based particles may change in the range of [0.85, 1.0]. To possibly reduce the influence of elongations, the particles whose elongations are in the range of [0.98, 1.0] were chosen. The packings of the irregular rockfill particles with different D_3 values are shown in Fig. 3.

2.2 DEM modeling

Many researchers have tried to model a particle with a complicated shape in DEM by overlapping circles (for 2D) or spheres (for 3D) with various sizes [25, 40]. In this study, each 2D particle was modeled by some overlapping circles that best fit the Fourier-based particle contour and meet the requirement of the shape features. Detailed descriptions of the method can be found in [44]. Note that the breakage effect of rockfill particles was not considered in this study. Figure 4 displays the typical pictures of a DEM-simulated virtual rockfill particle from a Fourier-based particle contour.

The well-recognized DEM program PFC^{2D} [45] was employed to carry out the numerical simulations. The simple linear contact model [45] was utilized for both particle–particle and particle–wall contacts, which has been previously demonstrated to be able to reproduce certain key features of rockfill material [46–48]. The microscale parameters used in the numerical simulations are provided in Table 1. The normal stiffness of inter-particle contacts k_n is calculated according to $k_n = 2rtE_c / (r_a + r_b)$, where t is the size of particles in the z direction (the simulations were carried out in the x–y plane) and its default value is 1 m, E_c represents the effective modulus, r_a and r_b are the radii of constituent sub-circles of two particles in contact,

Fig. 3 Packings of the irregular rockfill particles with different D_3 values



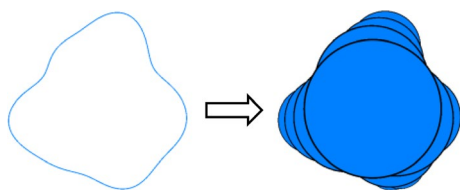


Fig. 4 A DEM-simulated virtual rockfill particle from a Fourier-based particle contour

Table 1 Microscale parameters used in the DEM simulations

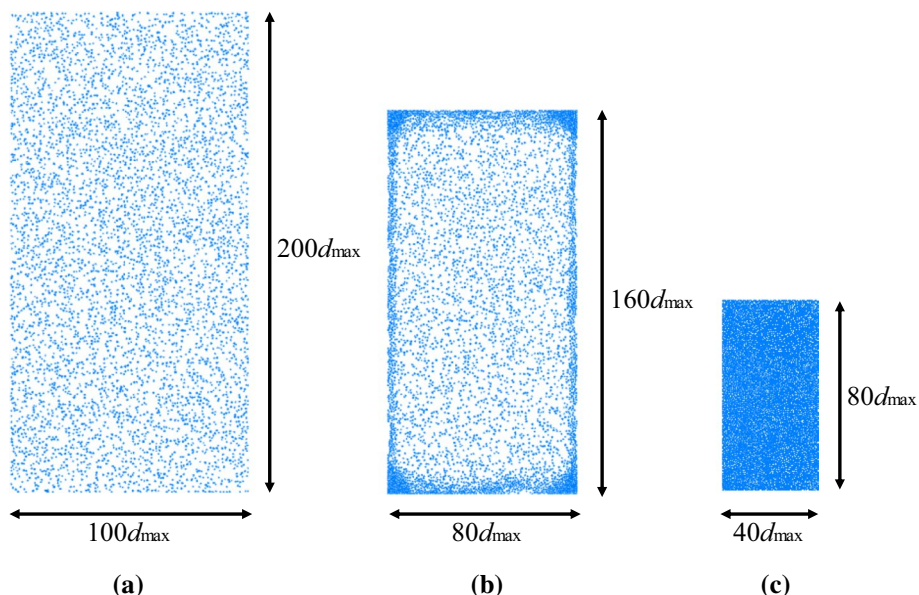
Parameter	Value
Particle density (kg/m^3)	2650
Inter-particle frictional coefficient	0.5
Wall-particle frictional coefficient	0
Normal stiffness of wall-particle contacts (N/m)	2×10^8
Effective modulus, E_c (Pa)	1×10^8
Stiffness ratio (k_n/k_s)	4/3
Damping factor	0.7

and r denotes the minimum between r_a and r_b . The k_n value approximates $1 \times 10^8 \text{ N/m}$ due to the small dispersity of the particle radius; this value is similar to the normal contact stiffness used in [15, 46]. The k_n/k_s value (k_s refers to the tangential contact stiffness) is within the range of (1.0, 1.5), which was suggested by Goldenberg and Goldhirsch [49] for real particulate materials. Hence, $k_n/k_s = 4/3$ was used in the present study.

As mentioned above, eight types of rockfill particles with different D_3 values ranging from 0.00 to 0.18 were considered. The sample generation process is described as follows.

Initially, 5000 rockfill particles with random directions were generated within a large rectangular region modeled by four rigid walls, with no contact. The same particle number was also used in [21] for exploring the effects of asphericity on the shear behaviors of granular material. Note that Wang and Gutierrez [8] and Huang et al. [12] studied the influence of the particle number on the numerical simulation results. They discovered that the particle number has only a slight effect on the stiffness and the peak shear strength of granular material. To eliminate long-range ordering, a weak size polydispersity was introduced. The equivalent diameters of the particles in each sample range from 0.16 to 0.24 m, with a uniform distribution. The gravitational acceleration and frictional coefficients of inter-particle and particle–wall were provisionally set to 0 to eliminate force gradients and gain isotropically dense samples. Then, the sample was subjected to isotropic compression with a small strain rate. At the same time, a servo-control mechanism ensured the required confining stress 200 kPa. Finally, the sample was believed to be balanced, as the ratio of the mean unbalanced force to the mean contact force was less than 10^{-5} and the stress of the walls was less than a tolerance of 0.5% compared with the required confining stress. Figure 5 shows snapshots of the sample generation process of the sample with $D_3=0.12$: (a) initial stage, (b) isotropic compression stage and (c) final stage. The sizes of all samples are approximately $9.5 \text{ m} \times 19 \text{ m}$ after preparation. To avoid the size effect, Jamiolkowski et al. [50] advised that the ratio of the sample size to the maximum particle size should be larger than 5, with an ideal ratio of 8. In these simulations, the ratios were approximately 40. The densest sample could be attained with frictionless particles during the sample generation [51, 52]. Thus, all samples with different D_3 values before shear were deemed to have an identical relative density, as outlined

Fig. 5 Sample generation: **a** initial stage, **b** isotropic compression stage and **c** final stage



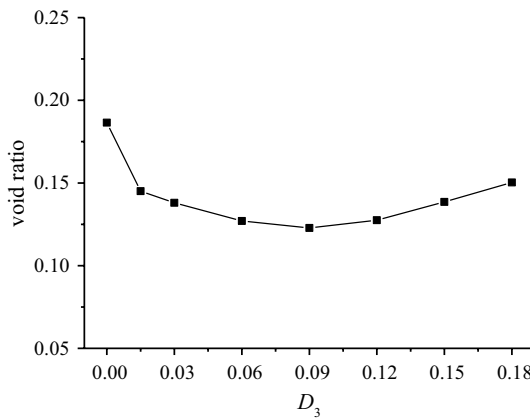


Fig. 6 Void ratios for all samples

in Azéma and Radjaï [26, 41], Lopez et al. [13, 14], and Gong and Liu [15, 25]. Figure 6 shows the void ratio against D_3 for all samples before shear. An analysis of Fig. 6 indicates that the void ratio depends on D_3 . The void ratio gradually decreases with increasing D_3 until it reaches the minimum value at $D_3=0.09$, and then the trend reverses with a further increase in D_3 .

All 2D numerical samples were ready to be sheared under a drained condition. Before the shear process, the inter-particle frictional coefficient was set to 0.5, which approximates the frictional coefficients of 0.47 used by Zhou et al. [47], 0.55 used by Ma et al. [48] and 0.54 used by Han et al. [53]. The frictional coefficient of particle–wall was maintained at zero during the shear process. The samples were subjected to a vertical compression by moving the top wall at a constant downward velocity, and a constant lateral confining stress 200 kPa was maintained by the servo-control mechanism. The shear rate should be so slow that the kinetic energy of particles can be negligible. This can be quantified by an inertia parameter I , which is defined as [54]:

$$I = \dot{\varepsilon}d\sqrt{\frac{\rho}{p'}} \quad (10)$$

where $\dot{\varepsilon}$ is the axial strain rate, d is the particle diameter, ρ is the particle density, and p' is the average stress. The quasi-static shear is ensured by the small I . It has been recommended that I should be below 2.5×10^{-3} in [55]. The constant velocity of the top wall was 0.05 m/s; thus, the inertia parameter I was less than 10^{-4} throughout the tests in this study.

3 Macroscopic behavior

In a 2D drained biaxial compression test, the effective mean stress p' and the deviatoric stress q are defined as follows:

$$p' = (\sigma_1 + \sigma_2)/2 \quad (11)$$

$$q = \sigma_1 - \sigma_2 \quad (12)$$

where σ_1 is the major principal stress, and σ_2 is the minor principal stress. The axial strain ε_1 and the volumetric strain ε_v can be estimated based on the boundary displacements:

$$\varepsilon_1 = (h_0 - h)/h_0 \quad (13)$$

$$\varepsilon_v = (v_0 - v)/v_0 \quad (14)$$

where h_0 is the initial height of the sample, h is the height of the sample at a specified state, v_0 is the initial volume of the sample, and v is the volume of the sample at a specified state. The volumetric compression is deemed to be positive in this study. The internal angle of friction (friction angle) φ , which indicates the shear strength of the non-cohesive granular material, is defined as

$$\sin \varphi = \frac{\sigma_1 - \sigma_2}{\sigma_1 + \sigma_2} = \frac{q}{2p'} \quad (15)$$

To investigate the responses of rockfill material at the critical state, all samples were sheared to the axial strain $\varepsilon_1=30\%$. With such a deformation, the typical conditions of the critical state, i.e., a constant stress and a constant volume, are approximately fulfilled. Figure 7 shows the stress ratio q/p' versus the axial strain ε_1 for all samples with various D_3 values. Obviously, all curves behave in a similar manner of dense non-cohesive granular material. That is, all curves exhibit a stiff response at the beginning of the shear phase; the stress ratio q/p' increases to a peak value at a small strain; then the stress ratio q/p' passes a peak value and gradually decreases to a relatively stable value. Figure 7 shows that the value of D_3 affects both the peak and critical shear strength.

The relationship between the peak and critical friction angles and D_3 is illustrated in Fig. 8. Note that the critical

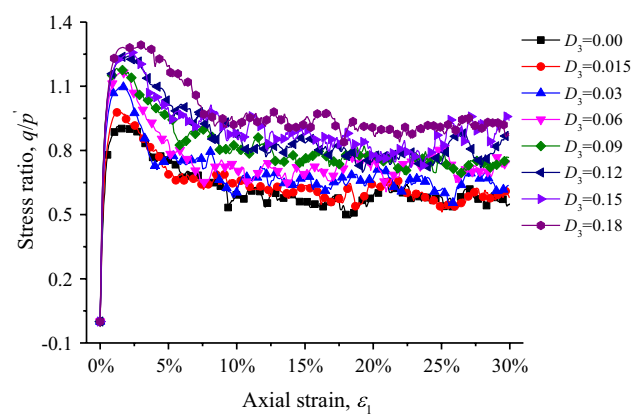


Fig. 7 Stress ratio–axial strain responses for all samples

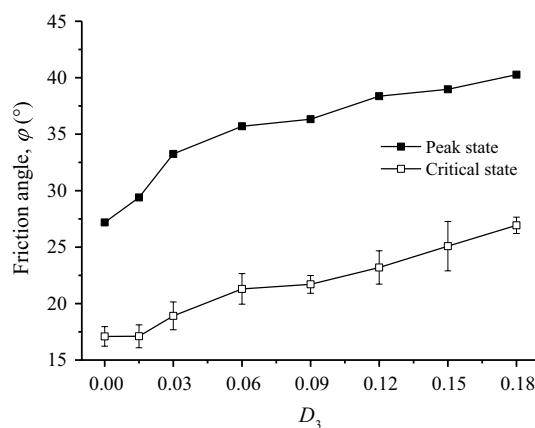


Fig. 8 Variations in the friction angles at the peak and critical states with respect to D_3

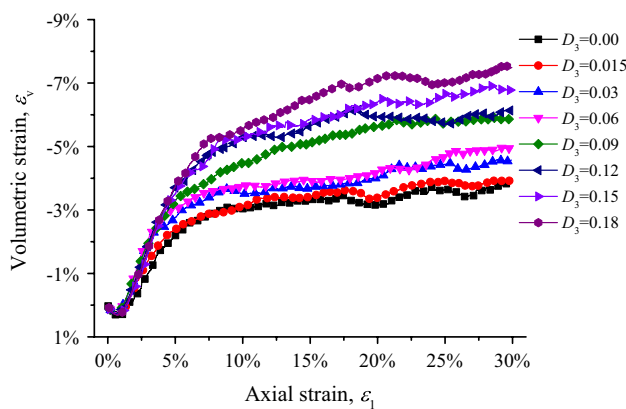


Fig. 9 Volumetric strain-axial strain responses for all samples

friction angles are calculated from the stress ratio q/p' at the axial strain ϵ_1 in the range of 20%–30% in consideration of the fluctuation in the stress ratio q/p' . The error bars in Fig. 8 represent the standard deviations of the friction angles at the critical state. As shown in Fig. 8, both the peak and critical friction angles increase with increasing D_3 . As D_3 increases from 0.00 to 0.18, the peak friction angle increases from 27.18° to 40.27° , and the critical friction angle increases by 9.84° . Figure 2 indicates that the roundness, circularity and regularity show a negative correlation with D_3 . From Fig. 8, it is inferred that both the peak and critical friction angles increase with a decrease in the roundness, circularity and regularity of rockfill particles.

Figure 9 displays the volumetric strain ϵ_v versus the axial strain ϵ_1 for all samples with various D_3 values. For all samples, the volumetric strain ϵ_v is initially positive, then gradually decreases, and finally reaches a relatively stable negative value. This behavior suggests that all the samples slightly

contract and then dilate. Meanwhile, the dilation is greater when the D_3 value is increased.

4 Microscopic behavior

4.1 Contact force

The external load of a particle system is transmitted through the contacts between particles, which forms the contact forces that are viewed as the significant factor influencing the mechanical properties of the particle system.

Normal contact forces contribute greatly to the shear strength [21]. To intuitively understand the physical mechanism of a particle system during the shear process, it is necessary to first visualize the normal contact force networks. Figure 10 shows maps of the normal contact force networks of samples with $D_3=0.00$, $D_3=0.06$ and $D_3=0.12$ at three characteristic states, namely, the initial, peak and critical states. The line thickness in Fig. 10 is proportional to the magnitude of the normal contact force. The quantitative index, i.e., the mean normal contact force $\langle f_n \rangle$, is introduced in this study. The value of $\langle f_n \rangle$ is given by the average of the normal contact force magnitudes over all inter-particle contacts in a sample. As observed, for a specified sample, at the initial state, the normal contact forces in the vertical direction and horizontal direction are nearly equal in magnitude. At the peak state, the mean normal contact force $\langle f_n \rangle$ obviously increases. In addition, the normal contact forces close to the vertical direction are clearly greater in magnitude, showing an obvious anisotropy. That is, the directions of strong force chains are approximately vertical. At the critical state, $\langle f_n \rangle$ reduces a little compared to the peak state, and the normal contact forces show a weaker anisotropy. At the same state, the mean normal contact force $\langle f_n \rangle$ is affected by D_3 . Specifically, $\langle f_n \rangle$ of the sample with $D_3=0.00$ is evidently greater than that of samples with $D_3=0.06$ and $D_3=0.12$. However, $\langle f_n \rangle$ of samples with $D_3=0.06$ and $D_3=0.12$ do not exhibit a significant difference.

The probability density of the normalized normal (tangential) contact force is of interest in this study, and is a crucial and typical quantity to study the contact force network [41, 56, 57]. The probability densities of normal contact forces f_n normalized by the mean normal contact force $\langle f_n \rangle$ at the peak state are shown in Fig. 11a, b. In Fig. 11a, when the normalized normal contact force $f_n/\langle f_n \rangle$ exceeds approximately 2.5, the probability densities of the latter several samples are significantly greater than that of the first sample. In Fig. 11b, when it is less than approximately 0.5, the probability density generally increases with increasing D_3 . The observations in Fig. 11a, b imply that the inhomogeneity [41] of normal contact forces generally increases with

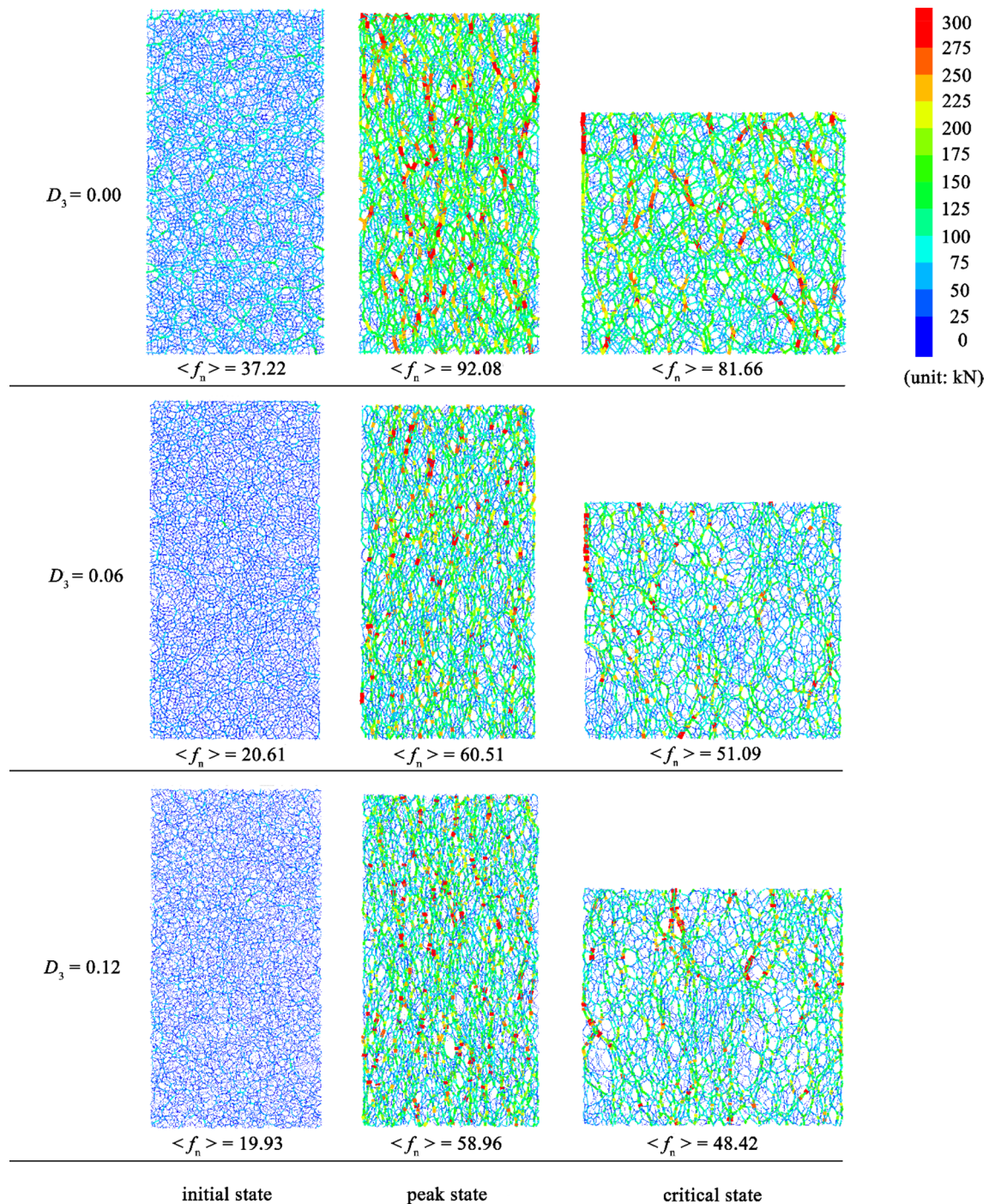


Fig. 10 Normal contact force networks at the initial, peak and critical states

increasing D_3 . Note that the features illustrated above are also observed in the probability density of the normalized tangential contact force, but are not shown here.

The polar diagram is adopted to visually depict the distributions of normal and tangential contact forces, where each data marker denotes a local average normal (tangential) contact force \bar{f}_n (\bar{f}_t) normalized average

normal contact force \bar{f}_0 . The local average normal (tangential) contact force \bar{f}_n (\bar{f}_t) is equal to the average of the magnitudes of normal (tangential) contact forces that belong to the direction interval of 10 degrees. \bar{f}_0 is defined as the average of the \bar{f}_n over 36 direction intervals. Note that \bar{f}_0 , \bar{f}_n , and $\langle f_n \rangle$ are three distinct concepts,

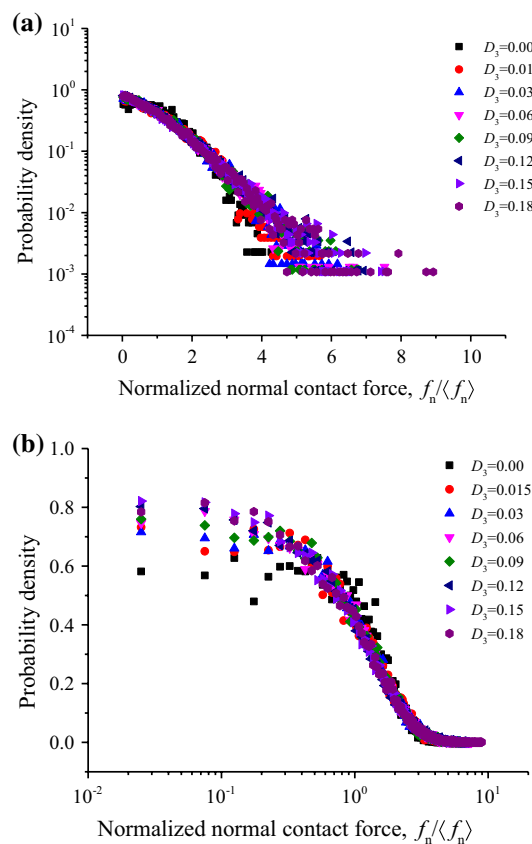


Fig. 11 Probability density of the normalized normal contact force in **a** log-linear and **b** linear-log scales at the peak state

and they are generally not equal except that the normal contact forces in all directions are equal in magnitude. Figure 12a, b show the distributions of normalized local average normal and tangential contact forces at the peak state for all samples. As shown in Fig. 12a, the shape of the distribution of normal contact forces resembles a peanut, indicating that normal contact forces in the vertical direction are much greater than normal contact forces in the horizontal direction. This is consistent with the phenomenon that the vertical contact forces are greater than the horizontal contact forces in contact force networks observed in Fig. 10. In addition, it is observed that the vertical \bar{f}_n/\bar{f}_0 slightly decreases with increasing D_3 , while the horizontal \bar{f}_n/\bar{f}_0 slightly increases with increasing D_3 . Remark that previous researchers have indicated that the horizontal contact forces are relatively small and provide lateral support for the propagation of relatively large contact forces. Alternatively, the shape of the distribution of tangential contact forces resembles a butterfly, as shown in Fig. 12b, indicating that tangential contact forces in the directions of $45^\circ + k \times 90^\circ$ ($k = 0, 1, 2, 3$) are obviously greater than those in the other directions. This corresponds with observations in Azéma et al. [56], Nguyen et al. [58],

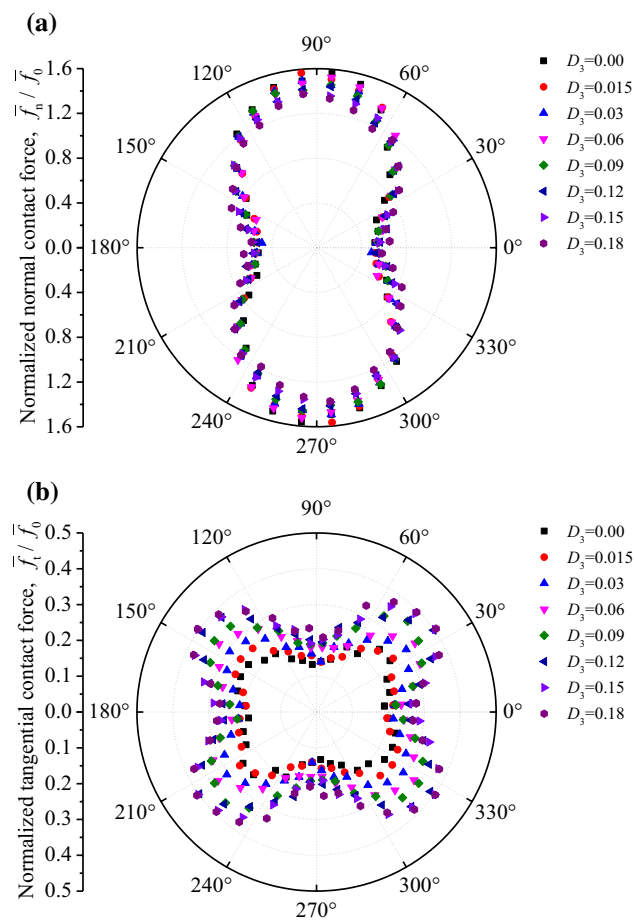


Fig. 12 Polar diagrams of normalized local average **a** normal and **b** tangential contact forces at the peak state

Rothenburg and Bathurst [59], and Yang and Dai [60]. In addition, with an increase in D_3 , the butterfly gradually becomes larger. Figure 12a, b indicate the anisotropies of normal and tangential contact forces, which will be discussed in the following section of ‘Fabric anisotropy’.

4.2 Coordination number and sliding contacts

The coordination number is an important index to quantify the internal structural characteristics of a particle system and has two definitions for multi-disk clumps. One definition refers to the number of particles in contact with a specified particle, and the other is the number of contacts belonging to a given particle [61]. In this study, we focus on the mean coordination number based on the second definition. Figure 13 illustrates the variations in the mean coordination number versus the axial strain. It can be seen that the mean coordination number initially decreases with increasing the axial strain, and then gradually stabilizes when the axial strain reaches approximately 10%. Furthermore, with an increase in D_3 , the mean coordination number gradually

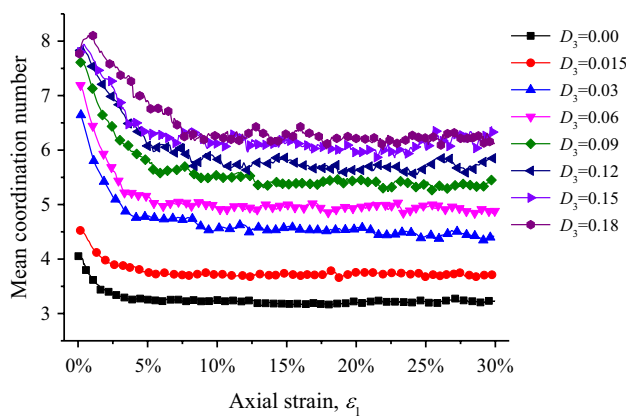


Fig. 13 Variations of the mean coordination number during the shear process

increases. The greater the mean coordination number is, the more notable the interlocking between particles is, resulting in a more stable particle system. Therefore, the shear strength at both the peak and critical states gradually increases with an increase in D_3 , as indicated in Fig. 7. As shown in Fig. 11b, the probability density of small $f_n/\langle f_n \rangle$ increases with increasing D_3 . This may be related to the fact that the mean coordination number increases with increasing D_3 . In the transmission of contact forces, the greater the contact number is, the more easily contact forces are dispersed.

To investigate the sliding contacts, the fiction sliding index $I_m = f_t / (\mu f_n)$ is introduced [21, 41], where f_t is the tangential contact force, μ is the frictional coefficient, and f_n is the normal contact force. In this study, contact sliding is believed to occur, when I_m is greater than 0.9999. Figure 14 displays the probability density of I_m at the peak state and the critical state (the corresponding axial strain is 30%). Clearly, the probability density decreases with increasing D_3 , as I_m is less than approximately 0.6, while the probability density presents an opposite trend, as I_m is greater than approximately 0.6. These results indicate that as D_3 increases, the quantity of weakly mobilized contacts decreases, whereas the quantity of strongly mobilized contacts increases. Figure 15 shows the variations in the percentage of sliding contacts with the axial strain. It can be seen that the percentage of sliding contacts sharply increases to a peak value, and then gradually decreases to a steady value. In addition, with an increase in D_3 , the percentage of sliding contacts increases. Estrada et al. [62] found that when relative motion occurs between particles in contact, the stronger anti-rotation ability of non-regular particles will force contacts to slide to adjust the overall deformation of the sample. Thus, an increase in the percentage of sliding contacts results from an increase in the anti-rotation ability of particles with increasing D_3 .

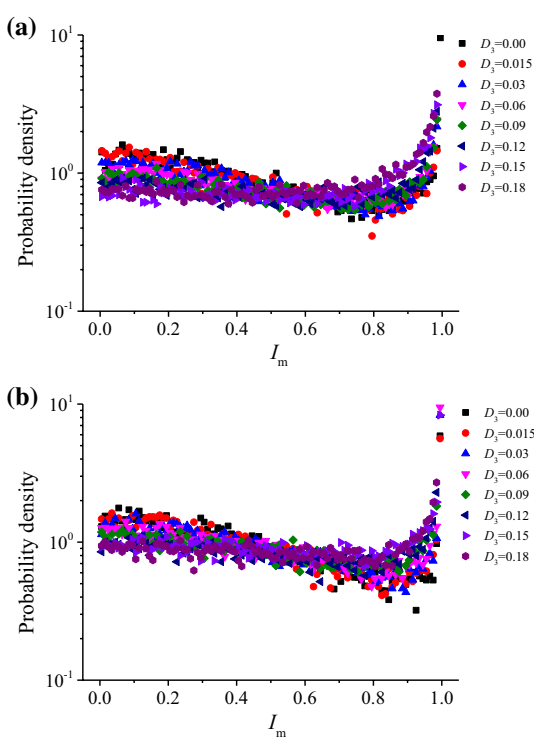


Fig. 14 Probability density of the sliding index: **a** the peak state and **b** the critical state

The evolution of the percentage of weak contacts ($f_n < \langle f_n \rangle$) during the shear process is shown in Fig. 16. As observed, the percentage of weak contacts initially falls off, and then gradually increases to a relatively steady value. Compared with strong contacts ($f_n \geq \langle f_n \rangle$), weak contacts play a dominant role in quantity, with a percentage of 55%–65%. In addition, the percentage of weak contacts generally increases with increasing D_3 , while the percentage of sliding contacts increases with increasing D_3 in Fig. 15.

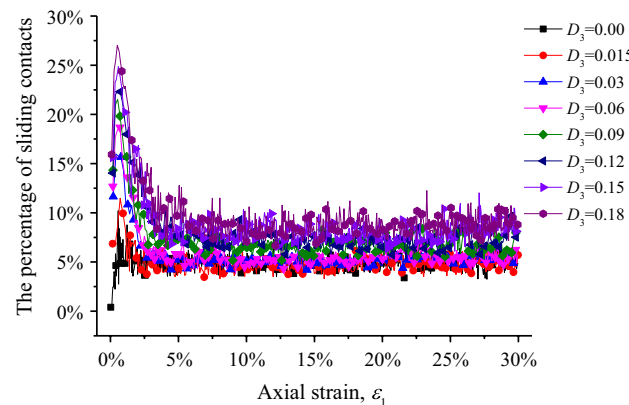


Fig. 15 Variations in the percentage of sliding contacts with the axial strain

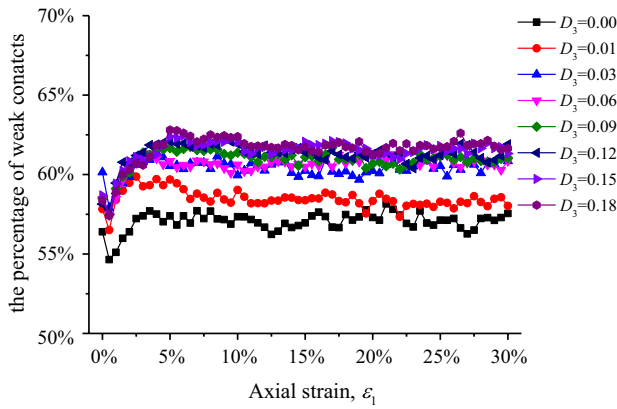


Fig. 16 Evolutions of the percentage of weak contacts during the shear process

A direct explanation is that contact sliding mainly occurs at weak contacts [25, 41]. Moreover, the change trend of the percentage of weak contacts with increasing D_3 in Fig. 16 is generally consistent with the results in Fig. 11b.

5 Fabric anisotropy

The macroscopic and microscopic properties presented above show the influences of D_3 on the mechanical behaviors of the particle system. To establish the relationship between the macroscopic and microscopic characteristics, fabric anisotropy is introduced in this section. The focus is on assessing the effects of D_3 on fabric anisotropy, together with the relationship between fabric anisotropy and shear strength.

5.1 Stress–force–fabric relationship

The entire contact network of the sample can be divided into m subnetworks. The stress tensor can be expressed as [16]:

$$\sigma_{ij} = \frac{N_c}{V} \sum_m \alpha_m \int_{\theta} \bar{f}_i^m(\mathbf{n}) \bar{d}_j^m(\mathbf{n}) E^m(\mathbf{n}) d\theta \quad (16)$$

where V represents the volume of the sample; $\alpha_m = \frac{N_c^m}{N_c}$; N_c^m and N_c are the amounts of contacts in the m th subnetwork and the entire contact network, respectively; $\bar{f}_i^m(\mathbf{n})$ is the i th component of the average contact force in the direction \mathbf{n} for the m th subnetwork; $\bar{d}_j^m(\mathbf{n})$ is the j th component of the average branch vector in the direction \mathbf{n} for the m th subnetwork; and $E^m(\mathbf{n})$ is the probability density of the contact direction in the direction \mathbf{n} for the m th subnetwork. $E^m(\mathbf{n})$ can be expressed as

$$E^m(\mathbf{n}) = \frac{1}{2\pi} \left(1 + \mathbf{a}_{ij}^{c,m} n_i n_j \right) \quad (17)$$

where $\mathbf{a}_{ij}^{c,m}$ is the second-order tensor to describe the orientational distributions of contacts. $\mathbf{a}_{ij}^{c,m}$ is given by the following expression derived in [63]:

$$\mathbf{a}_{ij}^{c,m} = 4\varphi_{ij}^{m'} \quad (18)$$

where $\varphi_{ij}^{m'}$ is the deviatoric tensor corresponding to φ_{ij}^m [64]. $\bar{f}_i^m(\mathbf{n})$ and $\bar{d}_j^m(\mathbf{n})$ are determined by the following second-order approximations:

$$\bar{f}_i^m(\mathbf{n}) = \overline{\bar{f}_0^{n,m}} (1 + \mathbf{a}_{kl}^{n,m} n_k n_l) n_i + \overline{\bar{f}_0^{n,m}} \left[\mathbf{a}_{ij}^{t,m} n_j - (\mathbf{a}_{kl}^{t,m} n_k n_l) n_i \right] \quad (19)$$

$$\bar{d}_j^m(\mathbf{n}) = \overline{\bar{d}_0^{dn,m}} (1 + \mathbf{a}_{kl}^{dn,m} n_k n_l) n_j + \overline{\bar{d}_0^{dn,m}} \left[\mathbf{a}_{ij}^{dt,m} n_i - (\mathbf{a}_{kl}^{dt,m} n_k n_l) n_j \right] \quad (20)$$

where $\mathbf{a}_{ij}^{n,m}$ and $\mathbf{a}_{ij}^{t,m}$ are the second-order tensors that characterize the orientational distributions of normal and tangential contact forces, respectively, and $\mathbf{a}_{ij}^{dn,m}$ and $\mathbf{a}_{ij}^{dt,m}$ are the second-order tensors that describe the orientational distributions of normal and tangential branch vectors, respectively. The four tensors can be determined via the following formulas:

$$\mathbf{a}_{ij}^{n,m} = \frac{4}{\overline{\bar{f}_0^{n,m}}} \mathbf{F}_{ij}^{n,m'} \quad \mathbf{a}_{ij}^{t,m} = \frac{4}{\overline{\bar{f}_0^{n,m}}} \mathbf{F}_{ij}^{t,m'} \quad (21)$$

$$\mathbf{a}_{ij}^{dn,m} = \frac{4}{\overline{\bar{d}_0^{dn,m}}} \mathbf{D}_{ij}^{dn,m'} \quad \mathbf{a}_{ij}^{dt,m} = \frac{4}{\overline{\bar{d}_0^{dn,m}}} \mathbf{D}_{ij}^{dt,m'} \quad (22)$$

where $\mathbf{F}_{ij}^{n,m'}$ and $\mathbf{F}_{ij}^{t,m'}$ are the deviatoric tensors corresponding to $\mathbf{F}_{ij}^{n,m}$ and $\mathbf{F}_{ij}^{t,m}$ respectively given by [64]; $\overline{\bar{f}_0^{n,m}} = \mathbf{F}_{ii}^{n,m}$ is the average normal contact force and is distinguished from the arithmetic mean normal contact force; $\mathbf{D}_{ij}^{dn,m'}$ and $\mathbf{D}_{ij}^{dt,m'}$ are the deviatoric tensors corresponding to $\mathbf{D}_{ij}^{dn,m}$ and $\mathbf{D}_{ij}^{dt,m}$, respectively, given by [64]; $\overline{\bar{d}_0^{dn,m}} = \mathbf{D}_{ii}^{dn,m}$ is the average normal branch vector and is differentiated from the arithmetic mean normal branch vector. After substituting Eqs. (17), (19) and (20) into (16), the stress tensor can be ultimately expressed as follows:

$$\sigma_{ij} = \frac{N_c \overline{\bar{f}_0^{n,m}} \overline{\bar{d}_0^{dn,m}}}{2V} \sum_m \xi_m \left(\delta_{ij} + \frac{\mathbf{a}_{ij}^{c,m} \mathbf{a}_{ij}^{n,m}}{2} \delta_{ij} + \frac{\mathbf{a}_{ij}^{c,m} + \mathbf{a}_{ij}^{n,m} + \mathbf{a}_{ij}^{t,m} + \mathbf{a}_{ij}^{dn,m} + \mathbf{a}_{ij}^{dt,m}}{2} \right) \quad (23)$$

where $\xi_m = \frac{\alpha_m \gamma_m}{\sum_m \alpha_m \gamma_m}$ is the weighting parameter; $\gamma_m = \frac{\overline{\bar{f}_0^{n,m}}}{\overline{\bar{f}_0^n}}$ and δ_{ij} is the Kronecker delta.

The effective mean stress p' and the deviatoric stress q can be given by $p' = \sigma_{ii}/2$ and $q = \sqrt{2\sigma'_{ij}\sigma'_{ij}}$ respectively, where σ'_{ij} is the deviatoric tensor corresponding to the stress tensor σ_{ij} . The fabric is deviatoric, so it is convenient to utilize the scalar a_*^m , attained from the invariant of every anisotropy tensor (i.e., $\mathbf{a}_{ij}^{c,m}, \mathbf{a}_{ij}^{n,m}, \mathbf{a}_{ij}^{t,m}, \mathbf{a}_{ij}^{dn,m}$ and $\mathbf{a}_{ij}^{dt,m}$), to describe the degree of fabric anisotropy, as follows:

$$a_*^m = \text{sign}(S_r) \sqrt{\frac{\mathbf{a}_{ij}^{*,m} \mathbf{a}_{ij}^{*,m}}{2}} \quad (24)$$

where a_*^m represents the anisotropic coefficients $a_c^m, a_n^m, a_t^m, a_{dn}^m$ and a_{dt}^m , corresponding to the five anisotropy tensors mentioned above; S_r is a normalized scalar of the double contraction of $\mathbf{a}_{ij}^{*,m}$ and σ'_{ij} , given by [64]. Then, the stress-force-fabric (SFF) relationship between q/p' and a_*^m (neglecting the product between a_c^m and a_n^m) is given by

$$q/p' = \sum_m \xi_m (a_c^m + a_n^m + a_t^m + a_{dn}^m + a_{dt}^m) \quad (25)$$

It is obvious that as $m=1$ in Eq. (25) for the entire contact network, the SFF relationship reduces to the formula as follows:

$$q/p' = a_c + a_n + a_t + a_{dn} + a_{dt} \quad (26)$$

When $m=2$ in Eq. (25) for the strong and weak contact networks, the SFF relationship reduces to the expression

$$q/p' = \xi_s (a_c^s + a_n^s + a_t^s + a_{dn}^s + a_{dt}^s) + \xi_w (a_c^w + a_n^w + a_t^w + a_{dn}^w + a_{dt}^w) \quad (27)$$

where ξ_s represents the weighting parameter of the strong contact network; a_t^s denotes the anisotropic coefficient of tangential contact forces in the strong contact network; and the meanings of the other symbols can be inferred accordingly.

5.2 Anisotropy of the entire contact network

The relationship between shear strength and fabric anisotropy for the entire contact network is established in Eq. (26). To validate the SFF relationship for the entire contact network, the macroscopic stress ratio q/p' from Eq. (15) is compared with the stress ratio q/p' from Eq. (26) in Fig. 17 for the sample with $D_3=0.12$. Clearly, the two kinds of stress ratios match, although there are slight deviations. The slight deviations are attributed to neglecting the tensor product of contact normal and normal contact force. The deviations disappear when the tensor product of contact normal and normal contact force is considered. Figure 17 indicates that the fabric anisotropy of a granular sample is the crucial origin of the shear strength. In addition, the anisotropic coefficients versus the axial strain are also plotted in Fig. 17

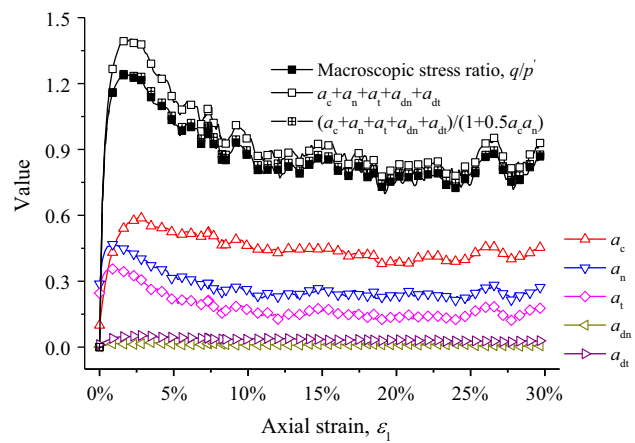


Fig. 17 Validation of the SFF relationship for the entire contact network

for the sample with $D_3=0.12$. Clearly, the anisotropic coefficient of contacts a_c plays a major role in providing the shear strength, which is consistent with the observations in Azéma and Radjaï [26, 41]. The anisotropic coefficient of normal contact forces a_n provides the second contribution to the shear strength, followed by the anisotropic coefficient of tangential contact forces a_t . In addition, the anisotropic coefficients of branch vectors a_{dn} and a_{dt} have very small contributions to the shear strength.

Figure 18a, b illustrate the evolution of the anisotropic coefficients with D_3 at the peak and critical states, respectively. Figure 18a shows that, at the peak state, a_n generally decreases and a_t increases with increasing D_3 , which agree with the anisotropic distributions of normal and tangential contact forces as indicated in Fig. 12a, b, respectively. a_c and a_{dt} increase as D_3 increases. At the critical state, the evolutions of anisotropic coefficients with D_3 are generally similar to those at the peak state. In addition, a_n at the critical state is obviously smaller than a_n at the peak state, showing that the anisotropy of normal contact forces at the critical state is weaker than that at the peak state. This is consistent with the observations in Fig. 10. One reasonable explanation for the variation trend in a_c and a_n versus D_3 is that an increasing a_c indicates that the number of contacts in the vertical direction increases and the number of contacts in the horizontal direction decreases. To maintain a constant confining pressure, the contact forces in the horizontal direction must increase, which results in the normal contact forces becoming less anisotropic; thus, a_n decreases. The SFF relationship enables us to grasp the microscopic mechanism of the macroscopic shear strength. With increasing D_3 , the shear strengths at the peak and critical states increase because of the increases in a_c, a_t and a_{dt} making up for the decrease in a_n .

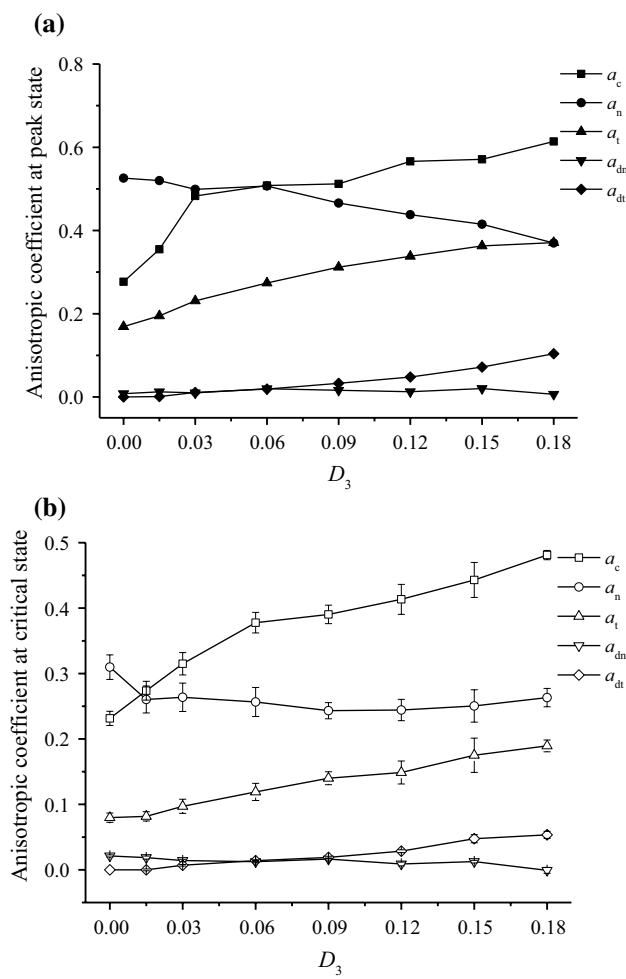


Fig. 18 Anisotropic coefficients of the entire contact network: **a** the peak state and **b** the critical state

5.3 Anisotropy of the strong and weak contact networks

The entire contact network was divided into the strong contact network and the weak contact network. The strong contact network carries normal contact forces larger than or equal to the mean normal contact force $\langle f_n \rangle$, whereas the weak contact network carries normal contact forces smaller than the mean normal contact force $\langle f_n \rangle$. To validate the SFF relationship for the strong and weak contact networks, the macroscopic stress ratio q/p' from Eq. (15) is compared to the stress ratio q/p' from Eq. (27) in Fig. 19 for the sample with $D_3=0.12$. Note that the anisotropic coefficients of the branch vectors, i.e., a_{dn}^s , a_{dt}^s , a_{dn}^w and a_{dt}^w , are neglected. Obviously, the two types of stress ratios agree well with each other. In addition, the contributions from the six anisotropies to q/p' versus the axial strain are also plotted in Fig. 19 for the sample with $D_3=0.12$. As observed, $\xi_s a_c^s$ is the major

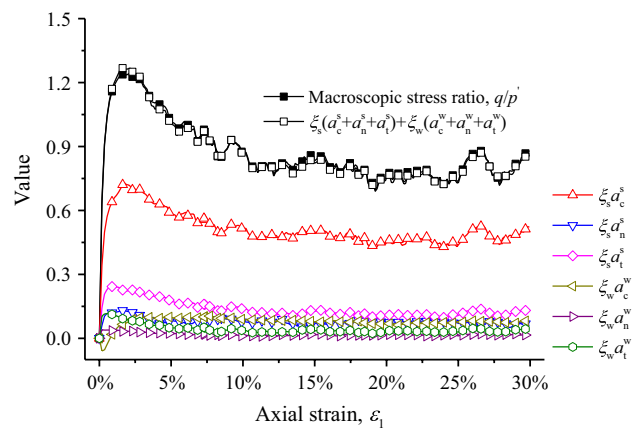


Fig. 19 Validation of the SFF relationship for the strong and weak contact networks

contributor to the shear strength, and the others have relatively small contributions.

The percentage contributions of the strong contact network and the weak contact network to the shear strength at the peak and critical states are quantified in Fig. 20. Obviously, the strong contact network is the major contributor to the shear strength, which has a percentage contribution beyond 80%. Furthermore, with an increase in D_3 , the percentage contribution of the weak contact network gradually increases. It should be noted that the variation in the percentage contribution of the weak contact network against D_3 is quite similar to the variation in the percentage of weak contacts against D_3 in Fig. 16.

Figure 21a, b present the evolutions of the anisotropic coefficients of the strong and weak contact networks with D_3 at the critical state. It is necessary to note that the anisotropic coefficients of the entire contact network may be different from the direct sum of the anisotropic coefficients of strong

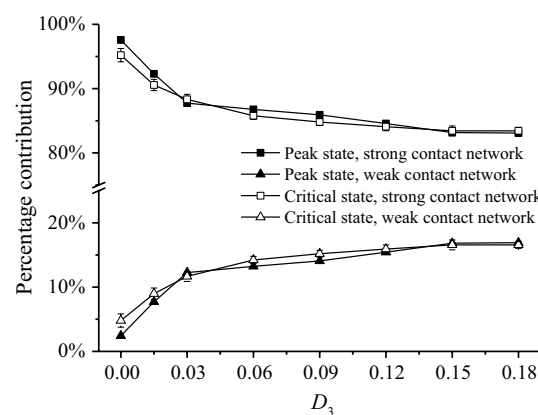


Fig. 20 Percentage contributions of the strong and weak contact networks at the peak and critical states

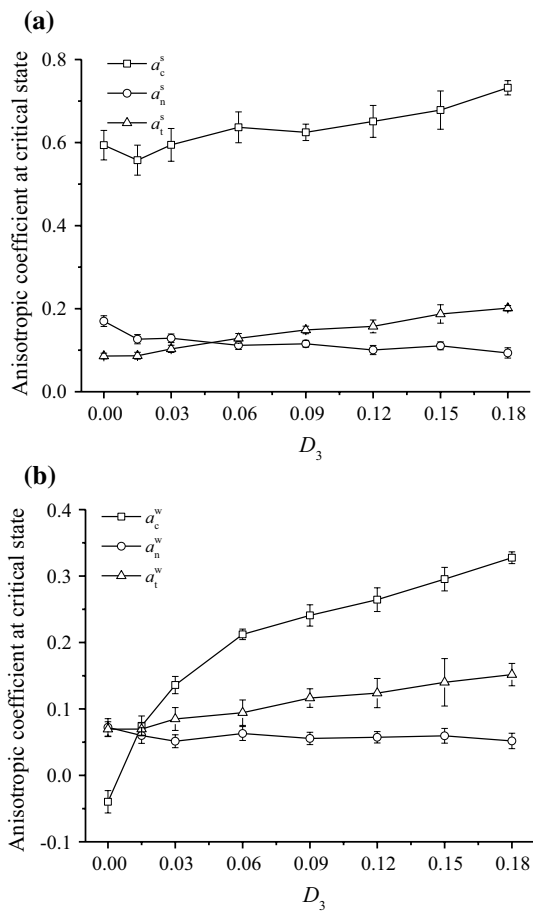


Fig. 21 Anisotropic coefficients at the critical state: **a** the strong contact network and **b** the weak contact network

and weak contact networks because of the tensor calculation. As shown in Fig. 21b, for $D_3=0.00$, the corresponding a_c^w is negative, which implies that the principal direction of weak contacts seems to be close to the horizontal direction. Obviously, in Fig. 21a, a_c^s generally decreases, whereas a_t^s increases with increasing D_3 . In Fig. 21b, both a_c^w and a_t^w increase with increasing D_3 . These findings demonstrate that the effects of D_3 on the anisotropy in the strong and weak contact networks in a sample are different. Note that, for all samples, the anisotropic coefficients of contacts and normal contact forces in the strong contact network are evidently larger than those in the weak contact network, which means that contacts and normal contact forces in the weak contact network are less anisotropic. This is consistent with the observations in Zhao and Zhou [21]. In addition, the value of a_c^s is much larger than the other anisotropic coefficients, i.e., a_n^s , a_t^s , a_c^w , a_n^w and a_t^w , and the weighting parameter ξ_s ranges from 0.70 to 0.75. These findings indicate that $\xi_s a_c^s$ is the dominant contributor to the shear strength of rockfill material.

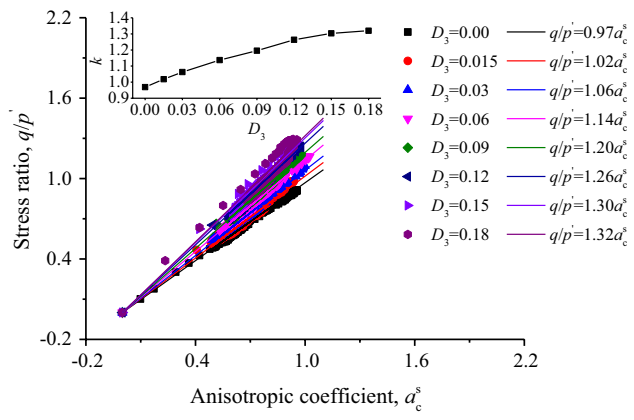


Fig. 22 A linear relationship between the macroscopic stress ratio q/p' and the anisotropic coefficient of contacts in the strong contact network

The variation in the macroscopic stress ratio q/p' versus anisotropic coefficient a_c^s is plotted in Fig. 22. Obviously, there is an interesting linear relationship between them as follows:

$$q/p' = k \times a_c^s \quad (28)$$

where k denotes the slope of the fitting line. This relationship holds true for the eight samples. The inset displays the relationship between k and D_3 . Clearly, k increases gradually with an increase in D_3 . When D_3 increases from 0.00 to 0.18, k increases from 0.97 to 1.32.

6 Conclusions

This report quantitatively analyzed the effects of particle shape on shear behaviors of rockfill material via 2D-DEM. The Fourier-based random generation method was applied to create virtual rockfill particles with different D_3 values, and all particles had almost equal elongations. Eight dense samples with different D_3 values, i.e., 0.00, 0.015, 0.03, 0.06, 0.09, 0.12, 0.15 and 0.18, were prepared by a given generation procedure, and then were subjected to shearing by numerical biaxial compression tests. The macroscopic behaviors, microscopic behaviors and fabric anisotropy of rockfill material were carefully investigated. The main conclusions are summarized as follows.

With increasing D_3 , the shear strength at the peak and critical states increases, and the sample shows a stronger dilatancy characteristic. At the initial state, the horizontal and vertical normal contact forces are generally equal. At the peak state, the mean normal contact force clearly increases, and the normal contact forces show an evident anisotropy. At the critical state, the mean normal contact force goes down a bit, and the normal contact forces show a weaker anisotropy. As D_3 increases, the inhomogeneity of normal contact forces

generally increases. The distributions of normalized local average normal and tangential contact forces for all samples in polar coordinates illustrate the anisotropies of normal and tangential contact forces. With increasing D_3 , the mean coordination number increases, indicating that the number of contacts increases. Thus, rockfill particles cannot easily rotate, resulting in an increase in the percentage of sliding contacts. The percentage of weak contacts increases because contact sliding occurs mainly at weak contacts. An increase in the percentage of weak contacts is consistent with an increase in the percentage contribution of the weak contact network to the shear strength; therefore, the percentage contribution of the strong contact network decreases gradually.

Fabric anisotropy analyses elucidate the essential origins of the shear strength. For the entire contact network, a_c and a_n play a major role in providing shear strength; a_t provides the third contribution, while a_{dn} and a_{dt} have very small contributions. With increasing D_3 , the shear strength at the peak and critical states increases due to the increases in a_c , a_t and a_{dt} compensating for the decrease in a_n . For the strong and weak contact networks, the strong contact network is the major contributor to the shear strength with a percentage contribution exceeding 80%. It is found that $\xi_s a_c^s$ is the dominant contributor to the shear strength of rockfill material. Interestingly, there is a satisfactory linear relationship between the macroscopic stress ratio q/p' and the anisotropic coefficient a_c^s , and the slope is affected by D_3 .

Acknowledgements This research was supported by the National Natural Science Foundation of China (Nos. 51478481 and 51809292), Beijing Municipal Science and Technology Project: Research and Application of Design and Construction Technology of Railway Engineering Traveling the Rift Valley (No. Z181100003918005) and the Fundamental Research Funds for the Central Universities of Central South University (No. 2018zzts195). The authors would like to express their appreciation for the financial assistance.

Compliance with ethical standards

Conflict of interest The authors declare no conflict of interest.

References

- Hartl, J., Ooi, J.Y.: Numerical investigation of particle shape and particle friction on limiting bulk friction in direct shear tests and comparison with experiments. *Powder Technol.* **212**(1), 231–239 (2011)
- Kozicki, J., Tejchman, J., Mroz, Z.: Effect of grain roughness on strength, volume changes, elastic and dissipated energies during quasi-static homogeneous triaxial compression using DEM. *Granul. Matter* **14**(4), 457–468 (2012)
- Azéma, E., Radjaï, F., Saint-Cyr, B., Delenne, J.Y., Sornay, P.: Rheology of three-dimensional packings of aggregates: microstructure and effects of nonconvexity. *Phys. Rev. E* **87**(5), 052205 (2013)
- Yagiz, S.: Brief note on the influence of shape and percentage of gravel on the shear strength of sand and gravel mixtures. *Bull. Eng. Geol. Environ.* **60**(4), 321–323 (2001)
- Chen, H.G., Wan, J.P.: The effect of orientation and shape distribution of gravel on slope angles in central Taiwan. *Eng. Geol.* **72**(1–2), 19–31 (2004)
- Li, Y.R., Huang, R.Q., Chan, L.S., Chen, J.: Effects of particle shape on shear strength of clay-gravel mixture. *KSCE J. Civil Eng.* **17**(4), 712–717 (2013)
- Cundall, P.A., Strack, O.D.L.: A discrete numerical model for granular assemblies. *Geotechnique* **29**(1), 47–65 (1979)
- Wang, J., Gutierrez, M.: Discrete element simulations of direct shear specimen scale effects. *Geotechnique* **60**(5), 395–409 (2010)
- Gu, X.Q., Yang, J.: A discrete element analysis of elastic properties of granular materials. *Granul. Matter* **15**(2), 139–147 (2013)
- Gu, X.Q., Yang, J., Huang, M.S.: DEM simulations of the small strain stiffness of granular soils: effect of stress ratio. *Granul. Matter* **15**(3), 287–298 (2013)
- Gu, X.Q., Huang, M.S., Qian, J.G.: DEM investigation on the evolution of microstructure in granular soils under shearing. *Granul. Matter* **16**(1), 91–106 (2014)
- Huang, X., Hanley, K.J., O'Sullivan, C., Kwok, F.C.Y.: Effect of sample size on the response of DEM samples with a realistic grading. *Particuology* **15**, 107–115 (2014)
- Lopez, R.D., Ekblad, J., Silfwerbrand, J.: Resilient properties of binary granular mixtures: a numerical investigation. *Comput. Geotech.* **76**, 222–233 (2016)
- Lopez, R.D., Silfwerbrand, J., Jelagin, D., Birgisson, B.: Force transmission and soil fabric of binary granular mixtures. *Geotechnique* **66**(7), 578–583 (2016)
- Gong, J., Liu, J.: Mechanical transitional behavior of binary mixtures via DEM: effect of differences in contact-type friction coefficients. *Comput. Geotech.* **85**, 1–14 (2017)
- Sufian, A., Russell, A.R., Whittle, A.J.: Anisotropy of contact networks in granular media and its influence on mobilised internal friction. *Geotechnique* **67**(12), 1067–1080 (2017)
- Hosseiniin, E.S.: Investigating the micromechanical evolutions within inherently anisotropic granular materials using discrete element method. *Granul. Matter* **14**(4), 483–503 (2007)
- Zhao, S.W., Zhou, X.W., Liu, W.H.: Discrete element simulations of direct shear tests with particle angularity effect. *Granul. Matter* **17**(6), 793–806 (2015)
- Ting, J.M., Meachum, L., Rowell, J.D.: Effect of particle shape on the strength and deformation mechanisms of ellipse-shaped granular assemblages. *Eng. Comput.* **12**(2), 99–108 (1995)
- Ng, T.T.: Particle shape effect on macro- and micro-behaviors of monodisperse ellipsoids. *Int. J. Numer. Anal. Methods* **33**(4), 511–527 (2009)
- Zhao, S.W., Zhou, X.W.: Effects of particle asphericity on the macro- and micro-mechanical behaviors of granular assemblies. *Granul. Matter* **19**(2), 38 (2017)
- Stahl, M., Konietzky, H.: Discrete element simulation of ballast and gravel under special consideration of grain-shape, grain-size and relative density. *Granul. Matter* **13**(4), 417–428 (2011)
- Altuhafi, F., O'Sullivan, C., Cavarretta, I.: Analysis of an image-based method to quantify the size and shape of sand particles. *J. Geotech. Geoenvir. Eng.* **139**(8), 1290–1307 (2013)
- Zhu, J.Y., Liang, Y.Y., Zhou, Y.H.: The effect of the particle aspect ratio on the pressure at the bottom of sandpiles. *Powder Technol.* **234**, 37–45 (2013)
- Gong, J., Liu, J.: Effect of aspect ratio on triaxial compression of multi-sphere ellipsoid assemblies simulated using a discrete element method. *Particuology* **32**, 49–62 (2017)

26. Azéma, E., Radjaï, F.: Stress-strain behavior and geometrical properties of packings of elongated particles. *Phys. Rev. E* **81**(5), 051304 (2010)
27. Sun, Y., Indraratna, B., Nimbalkar, S.: Three-dimensional characterisation of particle size and shape for ballast. *Geotech. Lett.* **4**, 197–202 (2014)
28. Yang, J., Luo, X.D.: Exploring the relationship between critical state and particle shape for granular materials. *J. Mech. Phys. Solids* **84**, 196–213 (2015)
29. Zhao, B.D., Wang, J.F.: 3D quantitative shape analysis on form, roundness, and compactness with μ CT. *Powder Technol.* **291**, 262–275 (2016)
30. Zheng, J., Hryciw, R.D.: Traditional soil particle sphericity, roundness and surface roughness by computational geometry. *Geotechnique* **65**(6), 494–506 (2015)
31. Zhao, L.H., Huang, D.L., Dan, H.C., Zhang, S.H., Li, D.J.: Reconstruction of granular railway ballast based on inverse discrete Fourier transform method. *Granul. Matter* **19**(4), 74 (2017)
32. Cho, G.C., Dodds, J., Santamarina, J.C.: Particle shape effects on packing density, stiffness, and strength: natural and crushed sands. *J. Geotech. Geoenviron. Eng.* **132**(5), 591–602 (2006)
33. Zheng, J.X., Hryciw, R.D.: Roundness and sphericity of soil particles in assemblies by computational geometry. *J. Comput. Civil Eng.* **30**(6), 04016021 (2016)
34. Ehrlich, R., Weinberg, B.: An exact method for characterization of grain shape. *J. Sediment. Petrol.* **40**(1), 205–212 (1970)
35. Meloy, T.P.: Fast fourier transforms applied to shape analysis of particle silhouettes to obtain morphological data. *Powder Technol.* **17**, 27–35 (1977)
36. Bowman, E.T.: Particle shape characterisation using Fourier descriptor analysis. *Geotechnique* **51**(6), 545–554 (2000)
37. Mollon, G., Zhao, J.D.: Fourier–Voronoi-based generation of realistic samples for discrete modelling of granular materials. *Granul. Matter* **14**(5), 621–638 (2012)
38. Mollon, G., Zhao, J.D.: Generating realistic 3D sand particles using Fourier descriptors. *Granul. Matter* **15**(1), 95–108 (2013)
39. Mollon, G., Zhao, J.D.: Characterization of fluctuations in granular hopper flow. *Granul. Matter* **15**(6), 827–840 (2013)
40. Liu, Z., Zhao, J., Mollon, G.: The influence of particle shape for granular media: a fourier-shape-descriptor-based micromechanical study. In: Proceedings of 3rd International Symposium on Geomechanics from Micro to Macro, Cambridge, England (2015)
41. Azéma, E., Radjaï, F.: Force chains and contact network topology in sheared packings of elongated particles. *Phys. Rev. E* **85**(3), 031303 (2012)
42. Suhr, B., Six, K.: Friction phenomena and their impact on the shear behaviour of granular material. *Comput. Part. Mech.* **4**(1), 23–34 (2017)
43. Zhao, T.T., Feng, Y.T., Wang, M.: An extended Greenwood–Williamson modelbased normal interaction law for discrete element modelling of spherical particles with surface roughness. *Int. J. Numer. Anal. Methods* **42**(14), 1624–1642 (2018)
44. Taghavi, R.: Automatic clump generation based on mid-surface. In: Proceedings of Continuum and Distinct Element Numerical Modeling in Geomechanics (2011)
45. Itasca: User's manual for PFC2D version PFC5.0. Itasca consulting Group Inc., Minneapolis (2014)
46. Alaei, E., Mahboubi, A.: A discrete model for simulating shear strength and deformation behaviour of rockfill material, considering the particle breakage phenomenon. *Granul. Matter* **14**(6), 707–717 (2012)
47. Zhou, W., Ma, G., Chang, X.L., Zhou, C.B.: Influence of particle shape on behavior of rockfill using a three-dimensional deformable DEM. *J. Eng. Mech.* **139**(12), 1868–1873 (2013)
48. Ma, G., Zhou, W., Chang, X.-L., Yuan, W.: Combined FEM/DEM modeling of triaxial compression tests for rockfills with polyhedral particles. *Int. J. Geomech.* **14**(4), 04014014 (2014)
49. Goldenberg, C., Goldhirsch, I.: Friction enhances elasticity in granular solids. *Nature* **435**(7039), 188–191 (2005)
50. Jamiolkowski, M., Kongskuprasert, L., Lo Presti, D.: Characterization of gravelly geomaterials. In: Proceedings of the Fifth International Geotechnical Conference, Bangkok, Thailand (2004)
51. Deluzarche, R., Cambou, B.: Discrete numerical modelling of rockfill dams. *Int. J. Numer. Anal. Methods* **30**(11), 1075–1096 (2006)
52. Abbireddy, C.O.R., Clayton, C.R.I.: Varying initial void ratios for DEM simulations. *Geotechnique* **60**(6), 497–502 (2010)
53. Han, H.X., Chen, W., Huang, B., Fu, X.D.: Numerical simulation of the influence of particle shape on the mechanical properties of rockfill materials. *Eng. Comput.* **34**(7), 2228–2241 (2017)
54. da Cruz, F., Emam, S., Prochnow, M., Roux, J.N., Chevoir, F.: Rheophysics of dense granular materials: discrete simulation of plane shear flows. *Phys. Rev. E* **72**(2), 021309 (2005)
55. Perez, J.C.L., Kwok, C.Y., O'Sullivan, C., Huang, X., Hanley, K.J.: Assessing the quasi-static conditions for shearing in granular media within the critical state soil mechanics framework. *Soils Found.* **56**(1), 152–159 (2016)
56. Azéma, E., Radjaï, F., Peyroux, R.: Force transmission in a packing of pentagonal particles. *Phys. Rev. E* **76**(1), 011301 (2007)
57. Estrada, N., Taboada, A., Radjaï, F.: Shear strength and force transmission in granular media with rolling resistance. *Phys. Rev. E* **78**(2), 021301 (2008)
58. Nguyen, D.H., Azéma, E., Sornay, P., Radjaï, F.: Effects of shape and size polydispersity on strength properties of granular materials. *Phys. Rev. E* **91**(3), 032203 (2015)
59. Rothenburg, L., Bathurst, R.J.: Analytical study of induced anisotropy in idealized granular materials. *Geotechnique* **39**(4), 601–614 (1989)
60. Yang, J., Dai, B.B.: Is the quasi-steady state a real behaviour? A micromechanical perspective. *Geotechnique* **61**(2), 175–183 (2011)
61. Markauskas, D., Kacianauskas, R., Dziugys, A., Navakas, R.: Investigation of adequacy of multi-sphere approximation of elliptical particles for DEM simulations. *Granul. Matter* **12**(1), 107–123 (2010)
62. Estrada, N., Azéma, E., Radjaï, F., Taboada, A.: Identification of rolling resistance as a shape parameter in sheared granular media. *Phys. Rev. E* **84**(1), 011306 (2011)
63. Kanatani, K.I.: Distribution of directional data and fabric tensors. *Int. J. Eng. Sci.* **22**(2), 149–164 (1984)
64. Guo, N., Zhao, J.D.: The signature of shear-induced anisotropy in granular media. *Comput. Geotech.* **47**, 1–15 (2013)

Publisher's Note Springer Nature remains neutral with regard to jurisdictional claims in published maps and institutional affiliations.